

Cite this: *J. Mater. Chem. A*, 2021, 9, 17821

Marked enhancement of electrocatalytic activities for gas-consuming reactions by bimodal mesopores†

Ling-Yu Dong, Xu Hu, Yun-Zhe Du, Rui Ge, Guang-Ping Hao * and An-Hui Lu *

Electrochemically catalytic conversions have attracted worldwide interest as promising routes to reach a sustainable and green energy cycle. The exploration of efficient electrocatalysts is one of the key tasks, in which the majority has focused on devising new active centers; however, mass transport that determines the reactant supply and the conductance of electrolyte ions and electrons is often overlooked. Here, we report on spatially locating active centers into parallelly bimodal mesopores by precisely engineering mesopore geometries, through which the contribution of the paralleled transport channels to the activity of gas-consuming reactions was quantitatively determined. Under identical conditions, bimodal mesoporous carbon-based electrocatalysts displayed a 2.9 times higher CO partial current density than monomodal mesoporous catalysts for CO₂-to-CO conversion in the kinetic region of -1.1 V vs. RHE. Likewise, the strong correlation between the activity enhancement and the bimodal mesopore geometry was verified for supported molecular catalysts and applicable to other gas-consuming reactions such as the O₂ reduction reaction. These encouraging results offer a fresh and general idea to advance electrocatalysts by pore geometry engineering on the mesoscale.

Received 24th June 2021
Accepted 22nd July 2021

DOI: 10.1039/d1ta05355h

rsc.li/materials-a

Introduction

With the concept of carbon neutrality reaching a consensus globally, electrochemical conversions have been increasingly postulated as important alternative routes for sustainable synthesis in view of the expected availability and low pricing of renewable electricity.¹ Among the electrochemical processes, the reduction reactions of CO₂ (CO₂RR), O₂ (ORR), N₂ (NRR) *etc.* are typical gas-consuming reactions, which occur at gas–liquid–solid tri-phase interfaces.² To ensure an effective conversion, an efficient coupling of protons and electrons with reactants around catalytically active centers is required.^{3,4} Thus, a continuous supply of feed gases (*e.g.*, CO₂ or O₂) and a high conductivity of protons and electrons to the active centers are the critical factors for high activity of an electrocatalytic system, while mass transport is essentially associated with the porous structure of electrocatalysts.

Porous carbon-based materials show excellent conductivity, controllable pore structure and hydrothermally stable frameworks, representing one of the most appealing classes of electrocatalysts.⁵ The majority of current efforts are taken on

designing new catalytic sites through surface functionalization such as heteroatom doping,^{6,7} defect engineering *etc.*^{8–13} However, the transport channels towards the active sites often show high tortuosity which suppresses internal diffusion, consequently leading to sluggish reaction kinetics. Independent research evidenced that a large proportion of narrow micropores displayed a low CO yield and Faraday efficiency (FE) in the catalytic CO₂RR.^{14,15} Similarly, nitrogen-coordinated cobalt sites in tortuous carbon pores were found partly inaccessible to ORR reactants, and thus decreased the utilization of the active sites.¹⁶

To make the transport channels more accessible, various methods have been investigated to increase the porosity and/or pore size^{17–20} For instance, by creating 2.45 times higher porosity (0.49 *vs.* 0.20 cm³ g⁻¹) than that of Fe, N-co doped porous carbon electrocatalysts, researchers found that a 4.4 times higher CO partial current density (j_{CO}) could be reached.²¹ Likewise, Dorotya *et al.*²² confirmed that mesoporous carbon-based electrocatalysts with the peak pore size distribution at 27 nm delivered a high FE_{CO} and j_{CO} . Meanwhile, it was found that the intrinsically active sites located in ordered mesoporous carbons led to superior catalytic activities due to improved reactant supply and highly accessible active sites.^{23–28} Overall, the available findings demonstrated that mass transfer limitations restrict the kinetics for the CO₂RR or ORR, while the reported carbon supports still lack pore geometry control over diffusion paths for molecules and solvated ions on the mesoscale.²⁹

State Key Laboratory of Fine Chemicals, Liaoning Key Laboratory for Catalytic Conversion of Carbon Resources, School of Chemical Engineering, Dalian University of Technology, Dalian 116024, P. R. China. E-mail: guangpinghao@dlut.edu.cn; anhuilu@dlut.edu.cn

† Electronic supplementary information (ESI) available. See DOI: 10.1039/d1ta05355h

Previous experimental and theoretical studies indicated that molecular diffusions in porous media were explicitly correlated with mesopore geometries.^{30,31} The transport channels in carbon-based catalysts are mainly in the forms of cavity, sphere, cube or their combinations, which often lower the diffusivities of guest molecules/ions compared to straight transport channels.^{18,23} Templated mesoporous carbons can be precisely tailor-made in terms of pore size, connectivity and geometry, making them ideal model catalysts for a wide range of electrochemical conversions. However, there are few efforts reported to unveil the influences of mesopore geometries of electrocatalysts on gas-consuming electroreduction reactions.

Herein, we reported that spatially locating active centers in terms of metal–nitrogen coordinated sites or Co–porphyrin molecular catalysts into highly accessible bimodal mesopores can be facilely achieved, enabling them to serve as efficient electrocatalysts for gas-consuming reactions. Exemplified by the CO₂RR conversions, the bimodal mesoporous electrocatalysts exhibited a 2.9 times higher CO geometric current density than monomodal inter-rod mesoporous catalysts; similar enhancement was also observed for a supported Co–porphyrin molecular catalyst as well as in selective O₂ electroreduction. The quantification of the pore geometry effects would benefit in-depth understanding of other electrocatalytic reactions beyond the gas-consuming reactions targeted here.

Experimental section

Chemicals and materials

All chemicals were purchased and used as received without further purification unless otherwise stated. CO₂ (99.99%) and Ar (99.9%) were purchased from Dalian Special Gases Co., Ltd. KHCO₃ (99.9%), phenanthroline monohydrate (Phen) and cobalt porphyrin (CoTPP) were purchased from Aladdin. Nickel(II) nitrate hexahydrate was purchased from Sinopharm Chemical Reagent Co., Ltd.

Synthesis of electrocatalysts

Bimodal and monomodal mesoporous carbon supports.

Bimodal mesoporous carbon (CMK-5, denoted as BMC) was prepared through a nanocasting method with mesoporous silica SBA-15 as the template, furfuryl alcohol (FA) as the carbon source and trimethylbenzene (TMB) as the pore-enlarging agent by following a known procedure.³² For the preparation of monomodal mesoporous carbon (CMK-3, denoted as MC), all the procedures were kept identical except for the absence of TMB.³³ For comparison, commercial activated carbon YP-50 was employed as the microporous carbon support.

Bimodal and monomodal mesoporous NiN_x electrocatalysts.

Typically, for the synthesis of NiN_x@BMC catalysts, a certain amount of Ni(NO₃)₂·6H₂O and Phen in stoichiometric proportions were dissolved in DI water, resulting in a Phen–Ni complex solution. Subsequently, 320 μL Phen–Ni complex was impregnated into BMC supports, which were dried at 50 °C overnight, and then treated in Ar at 300 °C and 900 °C for 1 h, respectively. The resultant composite was leached by hydrochloric acid (HCl,

4 M) to remove the Ni nanoparticles, followed by washing with water until neutralization. After drying, the NiN_x@BMC electrocatalyst was obtained with a nominal Ni loading of 4 wt%. By varying the loading of the Phen–Ni complex, the NiN_x@BMC samples with nominal Ni loadings of 2 and 8 wt% were prepared and denoted as NiN_x@BMC-L and NiN_x@BMC-H, respectively. Correspondingly, the specific surface area normalized Ni loadings for NiN_x@BMC-L, NiN_x@BMC and NiN_x@BMC-H were calculated to be 0.00883, 0.0172 and 0.0353 mg m⁻², respectively. Similarly, NiN_x@MC-L, NiN_x@MC and NiN_x@MC-H with the same normalized Ni loadings of 0.00883, 0.0172 and 0.0353 mg m⁻² were prepared, respectively. For comparison, a microporous electrocatalyst with a normalized Ni loading of 0.0172 mg m⁻² was prepared following the same procedures, denoted as NiN_x@microC.

Bimodal and monomodal mesoporous molecular electrocatalysts. A certain amount of CoTPP was dissolved in DMF at 120 °C. Then, CoTPP was supported on BMC *via* impregnation to achieve a nominal CoTPP loading of 0.2208 mg m⁻², and was dried at 120 °C for 2 h. Finally, the CoTPP@BMC electrocatalyst was obtained by drying in a vacuum at 100 °C for 24 h to remove the residual DMF. The preparation procedure for CoTPP@MC was identical to that of CoTPP@BMC but BMC was replaced with MC.

Characterization

N₂ sorption isotherms were collected at 77 K using a gas adsorption analyzer (Micromeritics, Tristar 3000). Powder X-ray diffraction (XRD) measurements were conducted with a PANalytical X'Pert3 powder diffractometer with Cu K α radiation ($\lambda = 1.5406 \text{ \AA}$). Transmission electron microscopy (TEM) was performed on a FEI TALOS F200X instrument. X-ray photoelectron spectroscopy (XPS) was conducted on an ESCALAB XI+, Thermo Ltd, with a monochromatic X-ray source (Mg K α). Raman spectra were recorded on a DL-2 microscopic Raman spectrometer with a laser (532 nm) as the emission light source. Inductively coupled plasma mass spectrometry (ICP-MS) was performed with an Agilent Technologies 7700 series instrument.

Electrochemical tests for the CO₂RR and ORR

Electrochemical measurements were performed using an electrochemical workstation (Ivium-n-Stat) without IR-compensation. The catalyst ink was prepared by mixing the catalyst with water, ethanol, and Nafion solution (5 wt%) to form a suspension with an active material loading of 6.6 mg mL⁻¹. For the CO₂RR test, a three-electrode system was applied with a working electrode, a saturated Ag/AgCl reference electrode, and a platinum sheet counter electrode. The reactant CO₂ was bubbled into a cathodic conductive electrolyte in a H-cell, and the FE was quantified by analyzing the content of gas products through online gas chromatography (Agilent, GC 7890B). After sonication for 60 min, 76 μL of the catalyst ink was pipetted onto carbon paper (1.0 × 1.0 cm²), which was vacuum dried overnight at 100 °C. The catalyst loading is *ca.* 0.5 mg cm⁻². The ORR activities of the as-prepared catalysts were studied using

a rotating ring disk electrode (RRDE; Ivium Technologies). A three-electrode system was built with an RRDE (glassy carbon (GC) disk + Pt ring), an Ag/AgCl reference electrode, and a platinum wire counter electrode. The above catalyst ink (*ca.* 6 μL) was dripped onto a pre-polished glassy carbon disk to achieve the working electrode with a catalyst loading of 0.3 mg cm^{-2} (disk area: 0.1256 cm^2 , ring area: 0.07854 cm^2). Before commencing ORR performance measurements, the RRDEs were pre-cycled with 40 cyclic voltammetry (CV) scans between 0.2 and 1.2 V *vs.* RHE in Ar-saturated 0.1 M KOH. The Pt ring was then electrochemically cleaned in the same potential range at a scan rate of 500 mV s^{-1} for 20 cycles. Linear sweep voltammetry (LSV) polarization measurements were performed in O_2 -saturated 0.1 M KOH at a scan rate of 5 mV s^{-1} with a rotation speed of 1600 rpm. The potential of the Pt ring was kept at 1.2 V *versus* RHE. Polarization curves in Ar-saturated electrolytes were also recorded as a reference. All potentials were converted to the reversible hydrogen electrode (RHE) reference scale using the equation: $E \text{ vs. RHE} = E \text{ vs. Ag/AgCl} + 0.0591 \times \text{pH} + 0.1981 \text{ V}$.

The H_2O_2 selectivity was calculated using the following equation:

$$\text{H}_2\text{O}_2 (\%) = 200 \times j_r / (j_d \times N + j_r)$$

where j_d and j_r are the currents obtained from the glassy carbon disk and Pt ring, respectively. N is the calibrated collection efficiency of RRDEs ($N = 0.385$).

The following equations were used to calculate the product-specific current density for H_2O_2 formation ($j_{\text{H}_2\text{O}_2}$) and H_2O formation ($j_{\text{H}_2\text{O}}$):

$$j_{\text{H}_2\text{O}_2} = j_r / (N \times A_{\text{geom}})$$

$$j_{\text{H}_2\text{O}} = j_d - j_{\text{H}_2\text{O}_2}$$

where A_{geom} is the surface area of the Pt ring.

The ORR electron transfer number (n) is determined from the following equation:

$$n = 4 \times j_d / (j_d + j_r / N)$$

Results and discussion

Two types of sophisticated mesoporous carbon models (BMC and MC) were employed for the investigation of the mesopore geometry influence on the electrocatalytic gas-consuming reduction reactions such as the CO_2RR or ORR. The grafting of the coordinated NiN_x centers in the mesopores of the BMC and MC was through incipient wetness impregnation and subsequent thermal treatment in an Ar atmosphere and leaching. By doing so, targeted location of active sites was achieved with a spatially specific feature (Fig. 1). On the MC, the NiN_x active centers are distributed in the inter-rod mesopores, while for the BMC, the active centers are located at both intra-tube and inter-tube mesopores. In addition to the coordinated NiN_x sites, the loading of larger porphyrin-type molecular

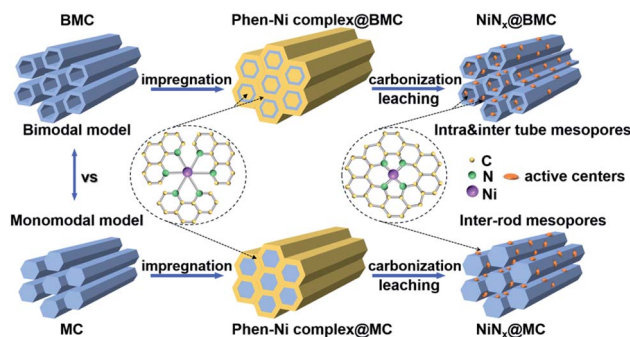


Fig. 1 Schematic of the synthesis of bimodal and monomodal mesoporous electrocatalysts $\text{NiN}_x\text{@BMC}$ and $\text{NiN}_x\text{@MC}$.

centers (CoTPP, $\sim 1.64 \text{ nm length} \times 1.64 \text{ nm width}$)³⁴ into the different mesopores was also explored. In principle, the ordered mesopores will promote rapid diffusion of reactants and products in/out of the active centers confined in the mesopores.³⁵ On the basis of the clear structure of the BMC and MC, we could extract in-depth information regarding the influence of mesopore geometry on their electrocatalytic performance.³⁶

The mesopore structure of the model carbon-supported electrocatalysts was investigated by N_2 physisorption and small angle XRD. The $\text{NiN}_x\text{@BMC}$ electrocatalyst exhibited a typical type-IV isotherm with a pronounced hysteresis loop at higher relative pressures, and the capillary condensation step corresponds to the filling with N_2 of small mesopores and wide mesopores in the P/P_0 range from 0.4 to 0.6, and 0.6 to 0.8, respectively (Fig. 2a).³⁷ In contrast, only a small hysteresis loop was observed in the P/P_0 range from 0.4 to 0.6 for $\text{NiN}_x\text{@MC}$. These results indicated the existence of mesopores in both samples and the formation of two types of mesopores at different length scales in $\text{NiN}_x\text{@BMC}$. Moreover, $\text{NiN}_x\text{@BMC}$ exhibited much higher adsorption capacity than $\text{NiN}_x\text{@MC}$ due to its bimodal mesopore geometry. The pore size distributions (PSDs) were determined by using the Barrett–Joyner–Halenda (BJH) theory based on the data points of the adsorption branch of the isotherms. The PSD curves (Fig. 2b) confirmed the bimodal mesopore systems of $\text{NiN}_x\text{@BMC}$ with the peak PSD centered at about 2.7 and 5.4 nm, corresponding to the inter-tube and the intra-tube mesopores, respectively. The $\text{NiN}_x\text{@MC}$ sample, however, exhibited only inter-rod mesopores with the peak PSD at 3.7 nm. In contrast, $\text{NiN}_x\text{@microC}$ exhibited a type-I isotherm, indicating its predominant microporous feature (Fig. S1†). The bimodal mesopore geometry of $\text{NiN}_x\text{@BMC}$ gave rise to a larger BET surface area of 1434 $\text{m}^2 \text{g}^{-1}$ and a total pore volume of 1.81 $\text{cm}^3 \text{g}^{-1}$ compared to those of $\text{NiN}_x\text{@MC}$ (830 $\text{m}^2 \text{g}^{-1}$, 0.92 $\text{cm}^3 \text{g}^{-1}$) and $\text{NiN}_x\text{@microC}$ (974 $\text{m}^2 \text{g}^{-1}$, 0.54 $\text{cm}^3 \text{g}^{-1}$) (Table S1†). In addition, the small angle XRD pattern (Fig. 2c) displayed a bump at around 0.9° and 1.1° , corresponding to the (100) and (110) reflections of hexagonal mesopores, respectively. The d -spacing calculated using the Bragg equation is 9.9 nm for the (100) plane of $\text{NiN}_x\text{@BMC}$. After NiN_x functionalization, the materials displayed very similar small angle XRD patterns, N_2 adsorption isotherms and

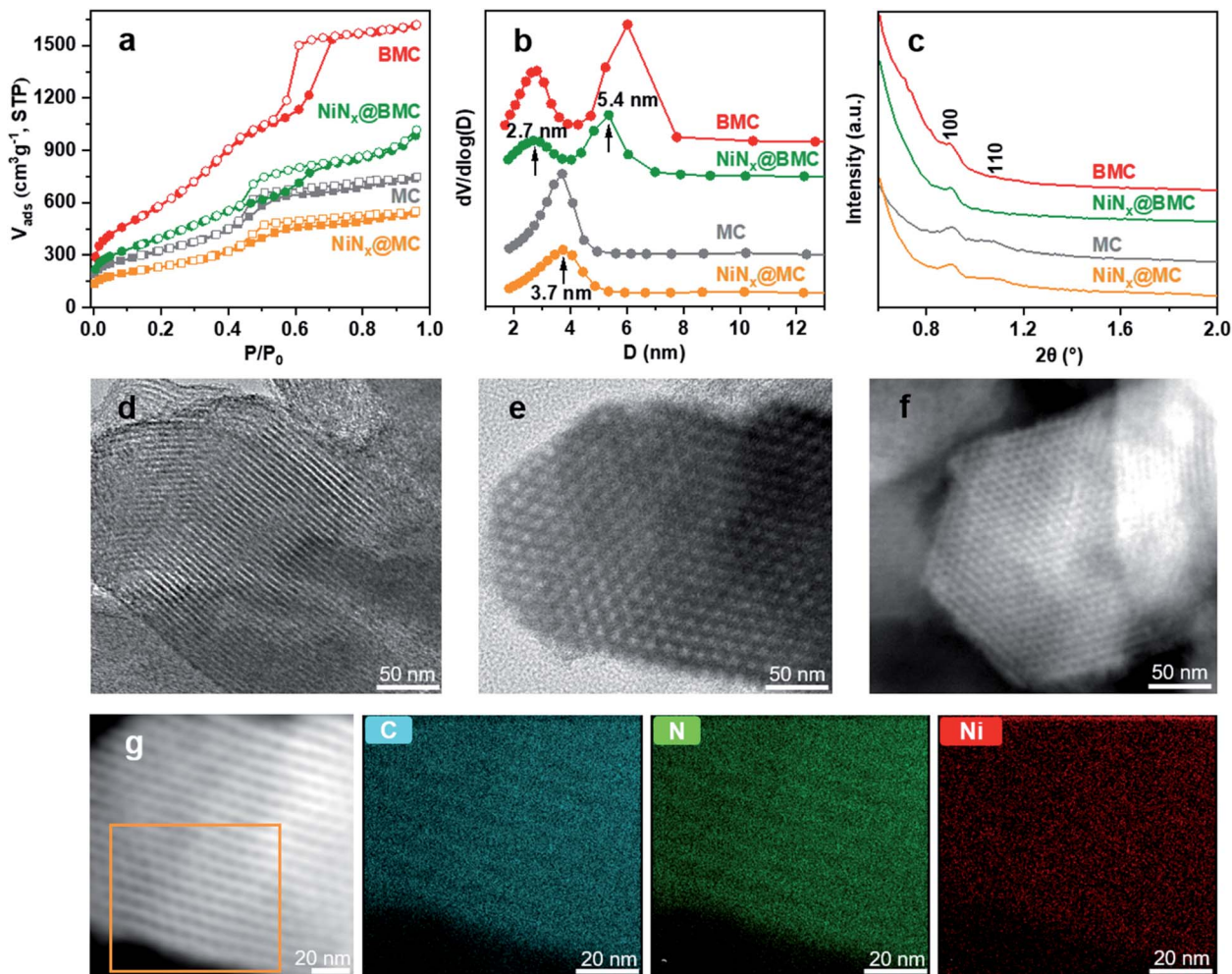


Fig. 2 Materials characterization of BMC and MC based electrocatalysts. (a) Nitrogen sorption isotherms, (b) pore size distributions, (c) small angle XRD patterns of MC, BMC, $\text{NiN}_x\text{@MC}$ and $\text{NiN}_x\text{@BMC}$; (d and e) bright-field TEM images, (f) dark-field scanning TEM image, (g) HAADF-STEM image and EDS mapping of $\text{NiN}_x\text{@BMC}$.

PSDs, indicating that the model mesopore geometry was not affected by the NiN_x incorporation.

The bimodal mesopores of $\text{NiN}_x\text{@BMC}$ were further studied by transmission electron microscopy (TEM; Fig. 2d–f, S2 and S3†). $\text{NiN}_x\text{@BMC}$ displayed alternating brightness and darkness, indicating a 2-D hexagonally ordered array of carbon tubes (Fig. 2d). The periodically ordered nanotube arrangement with a well-developed long-range order was further revealed from the light field (Fig. 2e) and dark field images in different directions (Fig. 2f). The center-to-center distance of adjacent channels in $\text{NiN}_x\text{@BMC}$ was around 9.6 nm, which is in line with the results from N_2 physisorption and small angle XRD. In addition, high-angle annular dark field scanning TEM (HAADF-STEM) and the corresponding energy-dispersive X-ray spectroscopy (EDS) element mapping further verified the homogeneous distribution of C, N and Ni atoms on the surface of $\text{NiN}_x\text{@BMC}$ (Fig. 2g). The $\text{NiN}_x\text{@BMC}$ electrocatalyst with a straight and bimodal mesopore geometry was expected to enhance mass transport for gas-consuming reactions compared to its rod-type counterpart ($\text{NiN}_x\text{@MC}$).³⁸

The wide-angle XRD patterns of $\text{NiN}_x\text{@BMC}$ and $\text{NiN}_x\text{@MC}$ showed relatively broad peaks centered at 24° and 44° (Fig. 3a and S4†), which correspond to the typical (002) and (100) planes of carbon materials, respectively. No metal-related diffraction peaks were observed in the XRD patterns, which confirms that the Ni species are in a highly dispersed phase. With increasing the Ni loading, the obtained $\text{NiN}_x\text{@BMC}$ started to show visible diffraction peaks which could be assigned to Ni nanoparticles. Raman spectra were then employed to investigate the carbon defects of BMC and MC after NiN_x functionalization. Both spectra revealed two typical bands at approximately 1335 cm^{-1} and 1585 cm^{-1} corresponding to the D and G bands of carbon materials, respectively (Fig. 3b).³⁹ The area ratio of D to G band for $\text{NiN}_x\text{@BMC}$ and $\text{NiN}_x\text{@MC}$ was almost the same (2.616 vs. 2.615), indicating similar concentrations of carbon defects in both catalysts. The surface chemical composition and elemental states in $\text{NiN}_x\text{@BMC}$ and $\text{NiN}_x\text{@MC}$ were investigated by X-ray photoelectron spectroscopy (XPS). The survey spectrum (Fig. S5†) revealed the existence of C, N, O and Ni elements in both samples, with the surface Ni content of

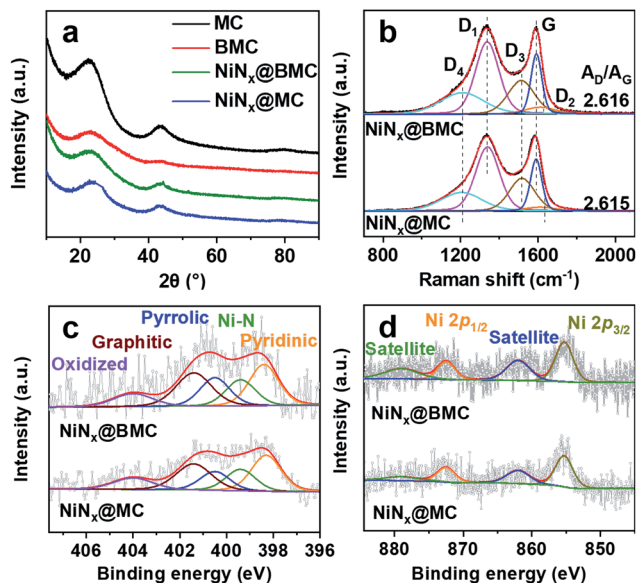


Fig. 3 Materials characterization of BMC and MC based electrocatalysts. (a) XRD patterns of MC, BMC and the final electrocatalysts; (b) Raman spectra; (c) high-resolution XPS N 1s and (d) Ni 2p spectra of $\text{NiN}_x\text{@BMC}$ and $\text{NiN}_x\text{@MC}$.

approximately 0.22 at% and 0.27 at% for $\text{NiN}_x\text{@BMC}$ and $\text{NiN}_x\text{@MC}$, respectively (Table S2[†]). The actual Ni loadings for $\text{NiN}_x\text{@BMC}$ and $\text{NiN}_x\text{@MC}$ were determined to be 0.77 and 0.50 wt% by ICP-MS analysis, which are in agreement with the specific surface area normalized Ni loadings. In addition, the N contents in $\text{NiN}_x\text{@BMC}$ and $\text{NiN}_x\text{@MC}$ are 1.44 at% and 2.18 at%, respectively. The N 1s (Fig. 3c) and Ni 2p spectra (Fig. 3d) both confirmed the formation of a Ni-N-C structure. The N 1s spectra of both catalysts can be deconvoluted into pyridinic-N (398.4 eV), Ni-N (399.4 eV), pyrrolic-N (400.5 eV), graphitic-N (401.5 eV), and oxidized-N (404 eV).^{40,41} The binding energy for nitrogen in coordinated Ni-N sites is around 399.4 eV, which is close to that of atomically dispersed Ni-N₃ or Ni-N₄ sites reported in the literature^{42,43} The binding energy of Ni 2p_{3/2} for both $\text{NiN}_x\text{@BMC}$ and $\text{NiN}_x\text{@MC}$ is around 855.2 eV, which is located between the metallic Ni⁰ (~852.6 eV) and Ni²⁺ (~856.0 eV) oxidation states.^{44–46} Thus, the XPS results for Ni 2p suggested that the Ni atoms in $\text{NiN}_x\text{@BMC}$ and $\text{NiN}_x\text{@MC}$ are likely in a low-valence state, which coincides with the characteristic of the Ni-N-C catalysts.^{45,46} The high-resolution C 1s spectrum (Fig. S6[†]) of the two samples indicated similar sp²-C (284.6 eV), sp³-C (285.3 eV), C-O (286.3 eV), C=O (287.6 eV), O=C-O (289.1 eV), and π-π* (291 eV).⁴⁷ Based on the above-mentioned characterization, it can be inferred that the two catalysts display similar physicochemical properties in terms of composition, defects, nature and density of intrinsic active sites *etc.*, while the main difference lies in the mesopore geometries.

The electrocatalytic CO₂RR performances of bimodal $\text{NiN}_x\text{@BMC}$ and monomodal $\text{NiN}_x\text{@MC}$ were first evaluated by LSV in Ar- and CO₂-saturated 0.5 M KHCO₃ electrolyte (Fig. S7[†]). The LSV curves indicated that both electrocatalysts exhibited a much higher current density in CO₂-saturated electrolyte,

indicating their activity for the CO₂RR. To further investigate the selectivity and CO production rates, constant potential electrolysis at applied potentials of -0.4 to -1.2 V was performed in a sealed H-type cell. It has been well proven that NiN_x sites are active coordinated non-precious metal centers for CO production. Consistently, CO was the major gas product and no liquid products could be detected for our electrocatalysts.

To unveil the role of mesopore geometry in selective CO₂ reduction to CO, we assessed the catalytic performances of different standards including areal and mass normalization. The areal activity refers to the activity normalized by the specific surface area. Alternatively, the mass activity refers to the activity normalized by the total mass of the electrocatalysts. In addition, the performance by normalizing to ECSA was first evaluated. For instance, by varying catalyst loading on carbon paper, electrocatalysts with similar double layer capacitances (C_{dl}) were obtained, with values of 8.72 and 8.92 mF cm⁻² (Fig. 4a) for $\text{NiN}_x\text{@BMC}$ and $\text{NiN}_x\text{@MC}$, respectively. This indicated similar accessibility of the reaction interface. Meanwhile, we applied the same specific surface area normalized Ni loading for both $\text{NiN}_x\text{@BMC}$ and $\text{NiN}_x\text{@MC}$, meaning that the two materials possessed the same areal density of the NiN_x sites. In this way, the CO₂RR performance essentially reflects the influences of different mesopore geometries. $\text{NiN}_x\text{@BMC}$ displayed a significantly larger ECSA-normalized specific activity (Fig. S8[†]), demonstrating that the enhanced CO₂ and proton supply was the main reason for the higher j_{CO} of $\text{NiN}_x\text{@BMC}$ than that of $\text{NiN}_x\text{@MC}$.⁴⁸

The $\text{NiN}_x\text{@BMC}$ catalyst also manifested a much superior geometric j_{CO} in the whole potential range tested (Fig. 4b), particularly showing 2.9 times higher j_{CO} (38.5 mA cm⁻²) than $\text{NiN}_x\text{@MC}$ (13.2 mA cm⁻²) at -1.1 V. Meanwhile, the CO₂ reduction onset potential of $\text{NiN}_x\text{@BMC}$ is at least 100 mV earlier than that of $\text{NiN}_x\text{@MC}$. More intriguingly, the j_{CO} started to decrease at more negative potentials (≤ -1.1 V) for $\text{NiN}_x\text{@BMC}$, whereas for $\text{NiN}_x\text{@MC}$ it started to reduce after only -0.9 V. We speculate that the excellent activity at higher potential was ascribed to the enhanced CO₂ diffusion over the highly interconnected bimodal mesopore geometry for $\text{NiN}_x\text{@BMC}$. The supply of CO₂ in the aqueous phase is often limited, particularly at high overpotentials, meanwhile the proton mobility has been evidenced to be faster than that of CO₂ molecules, which led to competitive hydrogen evolution reactions.⁴⁹ The performances of the state-of-the-art supported NiN_x electrocatalysts obtained under similar test conditions are compared in Table S3.† Notably, the highest production rate for $\text{NiN}_x\text{@BMC}$ (Fig. 4c) reached 712.5 μmol cm⁻² h⁻¹ in the kinetic region of -1.1 V, almost 3.0 times higher than that for $\text{NiN}_x\text{@MC}$ (241.2 μmol cm⁻² h⁻¹). The maximum j_{CO} of $\text{NiN}_x\text{@BMC}$ outperformed that of most of the reported catalysts under identical conditions. Furthermore, $\text{NiN}_x\text{@BMC}$ also displayed excellent CO selectivity, maintaining a high FE_{CO} (above 87%) over a wide potential range (from -0.6 to -1.0 V), with the highest FE_{CO} (94.8%) achieved at -0.9 V (Fig. 4d). The above results strongly evidenced that the unique bimodal mesopore geometry is in favour of catalytic activities for the CO₂RR to CO because of facilitated mass transfer.

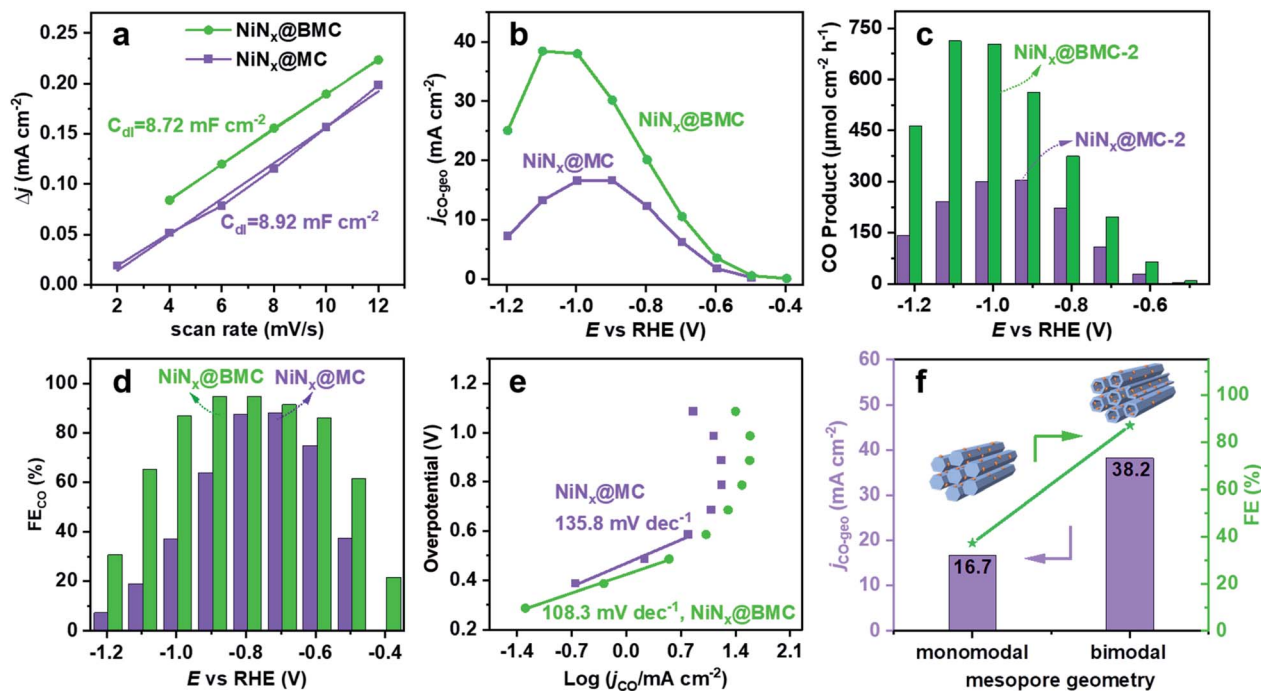


Fig. 4 Performance evaluation of the electrocatalysts. (a) Double layer currents as a function of the scan rates, calculated from the cyclic voltammograms, (b) CO partial current densities, (c) CO production rates, (d) CO Faradaic efficiencies, (e) Tafel plots, and (f) the comparison of CO₂RR performances of the bimodal and monomodal electrocatalysts at -1.0 V vs. RHE.

Furthermore, we verified the influence of the bimodal mesopores of electrocatalysts with varied Ni loadings. The CO₂RR performances of these samples with lower (NiN_x@BMC-L vs. NiN_x@MC-L) or higher (NiN_x@BMC-H vs. NiN_x@MC-H) Ni loadings in terms of the current density, FE and production rates of CO share a similar trend (Fig. S9 and S10[†]). NiN_x@BMC-L exhibited 3.1 times higher j_{CO} (27.5 mA cm^{-2}) and CO production rate ($515.2 \text{ } \mu\text{mol cm}^{-2} \text{ h}^{-1}$) than NiN_x@MC-L at -1.0 V. Furthermore, the FE_{CO} of NiN_x@BMC-L also reached nearly 100% at -0.7 V, markedly larger than that of NiN_x@MC-L (83%). With the loading of Ni increasing, Ni clusters started to appear which would improve the HER activity of NiN_x@BMC-H (Fig. S5[†]). Even in this case, the j_{CO} and FE_{CO} are still higher than those of NiN_x@MC-H. In addition, NiN_x@BMC sustained its high catalytic activity (20 mA cm^{-2}) for up to 24 h at -0.9 V (Fig. S11[†]), indicating its long-term stability. Tafel slopes of 108.3 and $135.8 \text{ mV dec}^{-1}$ were obtained for NiN_x@BMC and NiN_x@MC, respectively (Fig. 4e). The Nyquist plots (Fig. S12[†]) also showed a lower charge transfer resistance and Warburg diffusion resistance and faster electron kinetics for NiN_x@BMC, which all implied that the bimodal mesopore geometry can significantly accelerate the catalytic reaction kinetics (Fig. 4f). However, the microporous NiN_x@microC displayed a smaller j_{CO} of around 10.7 mA cm^{-2} , a lower CO production rate of around $195 \text{ } \mu\text{mol cm}^{-2} \text{ h}^{-1}$ and a higher Tafel slope of $165.2 \text{ mV dec}^{-1}$ over a wide range of potentials (Fig. S13[†]) than the mesoporous counterparts. These results strongly support the key role of the mesoporous transport channels.

Next, the CO₂RR performance by normalizing to the mass of active sites, *i.e.*, NiN_x sites, was evaluated. With the same weight

loading of active sites on the BMC and MC, we ensured that the total number of active sites was the same on both samples, but were dispersed more loosely on the BMC than on the MC (Fig. S14a[†]). To this end, the CO₂RR performance further reflects the influences of mass transport through the mesoporous channels and electrolyte ion diffusion. When the Ni loading is 2 wt%, the obtained NiN_x@BMC displayed a larger j_{CO} and FE_{CO} over the whole potential range (Fig. S14b and c[†]). The higher Ni loading up to 4 wt% improved the catalytic activity of both electrocatalysts. The j_{CO} is improved up to 38.2 mA cm^{-2} for NiN_x@BMC at -1.0 V, which is still 1.7 times higher than that of NiN_x@MC (22.9 mA cm^{-2}), while maintaining a 60.0% higher FE_{CO} (Fig. S14d and e[†]). This further indicated that the bimodal mesopore geometry of NiN_x@BMC is conducive to the faster mass transfer of reactants or products through the bimodal mesopores.

We further replaced the NiN_x active sites with a larger molecular catalyst, cobalt *meso*-tetraphenylporphyrin (CoTPP), which was loaded on the BMC and MC by impregnation (CoTPP@BMC and CoTPP@MC). The CoTPP@BMC catalyst showed improved activity and selectivity for CO production compared to CoTPP@MC. The maximum j_{CO} of 33 mA cm^{-2} was obtained at -1.1 V for CoTPP@BMC (Fig. 5a), which was 1.3 times higher than that of CoTPP@MC. Meanwhile, CoTPP@BMC showed higher FE_{CO} and CO production rates in a large potential range (Fig. 5b and c). Additionally, a C_{dl} value of 1.45 mF cm^{-2} was calculated for CoTPP@BMC, while for CoTPP@MC it is 1.50 mF cm^{-2} (Fig. S15[†]).

In addition to the model CO₂RR, we extended to the gas-consuming ORR which also occurs at the tri-phase with the

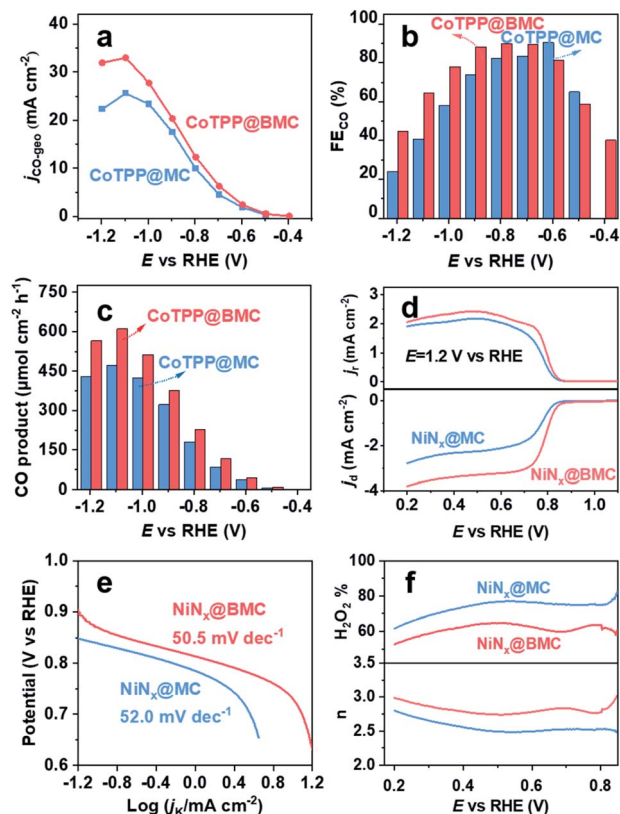


Fig. 5 Performance evaluations. (a) CO partial current density, (b) CO Faradaic efficiencies, (c) CO production rates for CoTPP@BMC and CoTPP@MC, (d) RRDE voltammograms for the ORR and H₂O₂ production, (e) Tafel plots, (f) the H₂O₂ selectivity of NiN_x@BMC and NiN_x@MC and the corresponding electron transfer number.

gaseous O₂ serving as the reactant. We assessed the ORR performance using a three-electrode rotating ring-disk electrode (RRDE) at 1600 rpm in an O₂-saturated 0.1 M KOH electrolyte. The ring electrode was held at 1.2 V to oxidize only the H₂O₂ formed at the disk electrode, which avoided other ORR currents at the ring electrode.^{50,51} Similarly, NiN_x@BMC delivered enhanced ORR kinetics compared to NiN_x@MC as revealed by the 63.2% higher disk current at 0.68 V and 0.868 V positive onset potentials (defined as a current density reaching -0.1 mA cm^{-2} , Fig. 5d), better than that of recently reported ORR electrocatalysts (Table S4[†]). Notably, a kinetic current density (j_k) of 21.2 mA cm^{-2} at 0.5 V was calculated for NiN_x@BMC, approximately 3.5 times higher than that of NiN_x@MC (6.1 mA cm^{-2}). This is a clear indication of the positive role of the bimodal mesopores. The Tafel slope of NiN_x@BMC is smaller than that of NiN_x@MC, which is probably due to the higher diffusion rate of oxygen in bimodal mesopores, indicating the higher ORR kinetics. Interestingly, both electrocatalysts displayed different Tafel slopes at different potential ranges. The lower Tafel slopes at higher potential are relevant to the reduction of oxygen to H₂O. However, at lower potential, H₂O₂ is preferentially produced. This phenomenon is typically ascribed to surface coverage effects. In other words, it is indicative of a reaction that does not accelerate quickly upon decreasing the applied potential, but rather associated with more reaction sites

becoming available. This observation is consistent with the previous findings (Fig. 5e).^{50–52} Note that the H₂O₂ current density of NiN_x@BMC displayed an evident increase over a wide potential range of 0.40–0.80 V, which reached around 2.43 mA cm^{-2} at 0.50 V, which is 1.12 times higher than that of NiN_x@MC.

In addition, we observed that the H₂O₂ selectivity of NiN_x@MC is higher than that of NiN_x@BMC (Fig. 5f). This revealed that the bimodal mesopore geometry benefited deeper reduction to H₂O possibly due to the sufficient O₂ and proton supply; however, on the monomodal mesoporous NiN_x@MC, the selective reduction to H₂O₂ is more preferential. In the potential range from 0.2 to 0.85 V, the electron transfer numbers were calculated to be 2.8–3.2 and 2.4–2.7 for NiN_x@BMC and NiN_x@MC, respectively (Fig. 5f), echoing the selectivity trend. These results reveal that the product distributions can potentially be tuned by tuning mesopore geometries. This is different from most of the available efforts that have been devoted to creating new active sites by doping heteroatoms, introducing transition metals, engineering defective sites *etc.* to alter product distributions.^{53,54} We expect that the mesopore geometry modulation could be a new method for selective electrochemical conversions not only for the CO₂RR and ORR targeted here, but also applicable to other electrocatalytic processes.

Conclusions

In summary, the bimodal mesoporous electrocatalysts were synthesized and investigated in electrochemical gas-consuming reactions as exemplified by selective CO₂-to-CO and O₂-to-H₂O₂ conversions. The bimodal mesopores were found effective in reactant gas and proton transport to catalytically active sites, which led to excellent kinetics and outstanding catalytic performance with markedly enhanced current density and production rates. The large contribution of the intra-tube transport channels of the bimodal mesopore systems to the catalytic performance was observed for the supported molecular catalysts and other electrochemical reactions such as the ORR as well. This study opens up a new perspective in boosting gas-consuming electrochemical reactions by pore geometry engineering on the mesoscale. Based on our experimental evidence and the literature results, we speculate that the unique bimodal structure would benefit other electrochemical reactions in liquid electrolytes. And further fundamental understanding and technological development of the bimodal catalysts are likely to make pore geometry modulation a general pathway for other electrochemical conversion processes.

Conflicts of interest

There are no conflicts to declare.

Acknowledgements

This work was financed by the National Natural Science Foundation of China (NSFC 21975037), the Liao Ning Revitalization

Talents Program (XLYC1807205) and the Fundamental Research Funds for the Central Universities of China (DUT18RC(3)075, DUT20LAB307).

References

- 1 Y. Yue, Y. Sun, C. Tang, B. Liu, Z. Ji, A. Hu, B. Shen, Z. Zhang and Z. Sun, *Carbon*, 2019, **154**, 108–114.
- 2 Y. Sa, C. Lee, S. Lee, J. Na, U. Lee and Y. Hwang, *Chem. Soc. Rev.*, 2020, **49**, 6632–6665.
- 3 R. Shi, J. Guo, X. Zhang, G. I. N. Waterhouse, Z. Han, Y. Zhao, L. Shang, C. Zhou, L. Jiang and T. Zhang, *Nat. Commun.*, 2020, **11**, 3028.
- 4 Z. Cai, Y. Zhang, Y. Zhao, Y. Wu, W. Xu, X. Wen, Y. Zhong, Y. Zhang, W. Liu, H. Wang, Y. Kuang and X. Sun, *Nano Res.*, 2019, **12**, 345–349.
- 5 X. Duan, J. Xu, Z. Wei, J. Ma, S. Guo, S. Wang, H. Liu and S. Dou, *Adv. Mater.*, 2017, **29**, 1701784.
- 6 C. Xu, A. Vasileff, Y. Zheng and S. Qiao, *Adv. Mater. Interfaces*, 2021, **8**, 2001904.
- 7 H. Cui, Y. Guo, L. Guo, L. Wang, Z. Zhou and Z. Peng, *J. Mater. Chem. A*, 2018, **6**, 18782–18793.
- 8 D. Xue, H. Xia, W. Yan, J. Zhang and S. Mu, *Nano-Micro Lett.*, 2021, **13**, 5.
- 9 Y. Wang, P. Han, X. Lv, L. Zhang and G. Zheng, *Joule*, 2018, **2**, 2551–2582.
- 10 H. B. Yang, S. Hung, S. Liu, K. Yuan, S. Miao, L. Zhang, X. Huang, H. Wang, W. Cai, R. Chen, J. Gao, X. Yang, W. Chen, Y. Huang, H. M. Chen, C. M. Li, T. Zhang and B. Liu, *Nat. Energy*, 2018, **3**, 140–147.
- 11 H. Yang, L. Shang, Q. Zhang, R. Shi, G. I. N. Waterhouse, L. Gu and T. Zhang, *Nat. Commun.*, 2019, **10**, 4585.
- 12 Yiliguma, Z. Wang, C. Yang, A. Guan, L. Shang, A. M. Al-Enizi, L. Zhang and G. Zheng, *J. Mater. Chem. A*, 2018, **6**, 20121–20127.
- 13 M. Abdinejad, C. Ferrag, M. N. Hossain, M. Noroozifar, K. Kerman and H. B. Kraatz, *J. Mater. Chem. A*, 2021, **9**, 12870–12877.
- 14 Y. Song, S. Wang, W. Chen, S. Li, G. Feng, W. Wei and Y. Sun, *ChemSusChem*, 2020, **13**, 293–297.
- 15 W. Liu, J. Qi, P. Bai, W. Zhang and L. Xu, *Appl. Catal., B*, 2020, **272**, 118974.
- 16 Y. Chen, C. Wang, Z. Wu, Y. Xiong, Q. Xu, S. Yu and H. Jiang, *Adv. Mater.*, 2015, **27**, 5010–5016.
- 17 T. Wang, C. Yang, Y. Liu, M. Yang, X. Li, Y. He, H. Li, H. Chen and Z. Lin, *Nano Lett.*, 2020, **20**, 5639–5645.
- 18 H. Yang, Y. Wu, Q. Lin, L. Fan, X. Chai, Q. Zhang, J. Liu, C. He and Z. Lin, *Angew. Chem., Int. Ed.*, 2018, **57**, 15476–15480.
- 19 J. Willkomm, E. Bertin, M. Atwa, J. Lin, V. Birss and W. E. Piers, *ACS Appl. Energy Mater.*, 2019, **2**, 2414–2418.
- 20 Y. Gong, L. Jiao, Y. Qian, C. Pan, L. Zheng, X. Cai, B. Liu, S. Yu and H. Jiang, *Angew. Chem., Int. Ed.*, 2020, **59**, 2705–2709.
- 21 C. Hu, S. Bai, L. Gao, S. Liang, J. Yang, S. Cheng, S. Mi and J. Qiu, *ACS Catal.*, 2019, **9**, 11579–11588.
- 22 D. Hursán, A. A. Samu, L. Janovák, K. Artyushkova, T. Asset, P. Atanassov and C. Janáky, *Joule*, 2019, **3**, 1719–1733.
- 23 D. Baek, K. Lee, J. Park, J. Kim, J. Lee, J. Lim, S. Lee, T. Shin, H. Jeong, J. Son, S. Kang, J. Kim and S. Joo, *Angew. Chem., Int. Ed.*, 2021, **60**, 1441–1449.
- 24 Z. Guo, N. Xiao, H. Li, Y. Wang, C. Li, C. Liu, J. Xiao, J. Bai, S. Zhao and J. Qiu, *J. CO₂ Util.*, 2020, **38**, 212–219.
- 25 J. Choi, J. Kim, P. Wagner, J. Na, G. G. Wallace, D. L. Officer and Y. Yamauchi, *J. Mater. Chem. A*, 2020, **8**, 14966–14974.
- 26 D. Dong, S. Xu, X. Shao, L. Hucker, J. Marin, T. Pham, K. Xie, Z. Ye, P. Yang, L. Yu, G. Parkinson and C. Li, *J. Mater. Chem. A*, 2017, **5**, 24098–24102.
- 27 B. Jia, Z. Xue, Q. Liu, Q. Liu, K. Liu, M. Liu, T. Chan, Y. Li, Z. Li, C. Su and G. Li, *J. Mater. Chem. A*, 2019, **7**, 15073–15078.
- 28 A. Hall, Y. Yoon, A. Wuttig and Y. Surendranath, *J. Am. Chem. Soc.*, 2015, **137**, 14834–14837.
- 29 S. Ringe, C. G. Morales-Guio, L. D. Chen, M. Fields, T. F. Jaramillo, C. Hahn and K. Chan, *Nat. Commun.*, 2020, **11**, 33.
- 30 F. Wei, T. Wang, X. Jiang, Y. Ai, A. Cui, J. Cui, J. Fu, J. Cheng, L. Lei, Y. Hou and S. Liu, *Adv. Funct. Mater.*, 2020, **30**, 2002092.
- 31 H. Liang, W. Wei, Z. Wu, X. Feng and K. Müllen, *J. Am. Chem. Soc.*, 2013, **135**, 16002–16005.
- 32 A. Lu, W. Li, W. Schmidt, W. Kiefer and F. Schüth, *Carbon*, 2004, **42**, 2939–2948.
- 33 A. Lu, W. Schmidt, A. Taguchi, B. Spliethoff, B. Tesche and F. Schüth, *Angew. Chem., Int. Ed.*, 2002, **41**, 3489–3492.
- 34 C. Wäckerlin, D. Chylarecka, A. Kleibert, K. Müller, C. Iacovita, F. Nolting, T. A. Jung and N. Ballav, *Nat. Commun.*, 2010, **1**, 61.
- 35 M. Qiao, Y. Wang, Q. Wang, G. Hu, X. Mamat, S. Zhang and S. Wang, *Angew. Chem., Int. Ed.*, 2020, **59**, 2688–2694.
- 36 Y. Wei, Z. Yang, G. Zhao and W. Yang, *J. Catal.*, 2019, **371**, 196–206.
- 37 K. Cheng, M. Virginie, V. V. Ordonsky, C. Cordier, P. A. Chernavskii, M. I. Ivantsov, S. Paul, Y. Wang and A. Y. Khodakov, *J. Catal.*, 2015, **328**, 139–150.
- 38 N. Farzin Nejad, E. Shams, M. K. Amini and J. C. Bennett, *Microporous Mesoporous Mater.*, 2013, **168**, 239–246.
- 39 X. Lu, T. Tan, Y. Ng and R. Amal, *Chem.–Eur. J.*, 2016, **22**, 11991–11996.
- 40 Y. Cheng, S. Zhao, B. Johannessen, J. Veder, M. Saunders, M. R. Rowles, M. Cheng, C. Liu, M. F. Chisholm, R. De Marco, H. Cheng, S. Yang and S. P. Jiang, *Adv. Mater.*, 2018, **30**, 1706287.
- 41 T. Zheng, K. Jiang, N. Ta, Y. Hu, J. Zeng, J. Liu and H. Wang, *Joule*, 2019, **3**, 265–278.
- 42 Y. Gong, L. Jiao, Y. Qian, C. Pan, L. Zheng, X. Cai, B. Liu, S. Yu and H. Jiang, *Angew. Chem., Int. Ed.*, 2020, **59**, 2705–2709.
- 43 C. Yan, H. Li, Y. Ye, H. Wu, F. Cai, R. Si, J. Xiao, S. Miao, S. Xie, F. Yang, Y. Li, G. Wang and X. Bao, *Energy Environ. Sci.*, 2018, **11**, 1204–1210.
- 44 X. Rong, H. Wang, X. Lu, R. Si and T. Lu, *Angew. Chem., Int. Ed.*, 2020, **59**, 1961–1965.

- 45 W. Xiong, H. Li, H. Wang, J. Yi, H. You, S. Zhang, Y. Hou, M. Cao, T. Zhang and R. Cao, *Small*, 2020, **16**, 2003943.
- 46 K. Jiang, S. Siahrostami, T. Zheng, Y. Hu, S. Hwang, E. Stavitski, Y. Peng, J. Dynes, M. Gangisetty, D. Su, K. Attenkofer and H. Wang, *Energy Environ. Sci.*, 2018, **11**, 893–903.
- 47 N. I. Kovtyukhova, T. E. Mallouk, L. Pan and E. C. Dickey, *J. Am. Chem. Soc.*, 2003, **125**, 9761–9769.
- 48 H. Chen, Z. Li, Z. Zhang, K. Jie, J. Li, H. Li, S. Mao, D. Wang, X. Lu and J. Fu, *Ind. Eng. Chem. Res.*, 2019, **58**, 15425–15431.
- 49 J. Wu, R. Yadav, M. Liu, P. P. Sharma, C. Tiwary, L. Ma, X. Zou, X. Zhou, B. I. Yakobson, J. Lou and P. M. Ajayan, *ACS Nano*, 2015, **9**, 5364–5371.
- 50 X. Guo, X. Jia, P. Song, J. Liu, E. Li, M. Ruan and W. Xu, *J. Mater. Chem. A*, 2017, **5**, 17470–17475.
- 51 K. Dong, J. Liang, Y. Wang, Z. Xu, Q. Liu, Y. Luo, T. Li, L. Li, X. Shi, A. M. Asiri, Q. Li, D. Ma and X. Sun, *Angew. Chem., Int. Ed.*, 2021, **60**, 10583–10587.
- 52 J. Wu, A. Mehmood, G. Zhang, S. Wu, G. Ali and A. Kucernak, *ACS Catal.*, 2021, **11**, 5035–5046.
- 53 C. Tang, L. Chen, H. Li, L. Li, Y. Jiao, Y. Zheng, H. Xu, K. Davey and S. Qiao, *J. Am. Chem. Soc.*, 2021, **143**, 7819–7827.
- 54 K. Jiang, S. Back, A. J. Akey, C. Xia, Y. Hu, W. Liang, D. Schaak, E. Stavitski, J. K. Nørskov, S. Siahrostami and H. Wang, *Nat. Commun.*, 2019, **10**, 3997.